PHYSICAL REVIEW B **76**, 064117 (2007)

Role of micropipes in the formation of pores at foreign polytype boundaries in SiC crystals

M. Yu. Gutkin
Institute of Problems of Mechanical Engineering, Russian Academy of Sciences, 199178 St. Petersburg, Russia and Department of Metal Physics and Computer Technologies, St. Petersburg State Polytechnical University, 195251 St. Petersburg, Russia

A. G. Sheinerman
Institute of Problems of Mechanical Engineering, Russian Academy of Sciences, 199178 St. Petersburg, Russia

T. S. Argunova
Ioffe Physico-Technical Institute, Russian Academy of Sciences, 194021 St. Petersburg, Russia and Department of Materials Science and Engineering, Pohang University of Science and Technology, San 31 Hyoja-dong, Namku, Pohang 790-784, Korea

J. M. Yi and J. H. Je*
X-ray Imaging Center, Department of Materials Science and Engineering, Pohang University of Science and Technology, San 31 Hyoja-dong, Namku, Pohang 790-784, Korea

S. S. Nagalyuk and E. N. Mokhov
Ioffe Physico-Technical Institute, Russian Academy of Sciences, 194021 St. Petersburg, Russia

G. Margaritondo
Institute de Physique Appliquée, Ecole Polytechnique Fédérale de Lausanne, CH-1015 Lausanne, Switzerland

Y. Hwu
Institute of Physics, Academia Sinica, Nankang, 11529 Taipei, Taiwan, Republic of China

(Received 18 January 2007; revised manuscript received 13 March 2007; published 23 August 2007)

The role of micropipes in pore formation in SiC crystals with foreign polytype inclusions is studied by means of synchrotron phase sensitive radiography, optical and scanning electron microscopies, and color photoluminescence. The pores at the inclusion boundaries are revealed, and their shapes and locations are analyzed. It is found that the pores arise due to the attraction of micropipes by the foreign polytype interfaces, followed by micropipe coalescence. The observed pores have tubular or slit shapes. Tubular pores nucleate at the inclusion corners, where the inclusion-associated stresses are concentrated. Slit pores spread between them and follow the shape of the inclusion boundaries. We explain the observations within a two-dimensional model of elastic interaction between micropipes and inclusion boundaries, which accounts for free surfaces of micropipes.

DOI: 10.1103/PhysRevB.76.064117 PACS number(s): 61.72.Lk, 61.72.Bb, 61.72.Ff

I. INTRODUCTION

An interesting feature of silicon carbide is its ability to crystallize into various polytypic structures differing in the stacking sequence in one direction. The electronic properties of SiC can widely vary depending on its polytypic structure. However, the controlled formation of a designed SiC polytype, either a bulk crystal or a layer, is difficult. For SiC crystals grown by the modified Lely technique,[1] the polytype occurrence and stability depend on the growth conditions and orientation of the substrate,[2–6] as well as on the probability of formation of singular faces during growth.[7] Even though the conditions for stable growth of a single polytype were developed,[2–6,8] uncontrolled formation of inclusions of other polytypes might occur. At the boundaries of foreign polytype inclusions, lattice defects are generated and lattice tilts are produced.[9] Since high-quality SiC wafers are required for SiC-based electronic devices, it is of special interest to elucidate the mechanisms for defect formation at the foreign polytype boundaries in SiC crystals.

Apart from dislocations, micropipes (MPs), cylindrical pores that generally contain dislocations with giant Burgers vectors,[10] were frequently observed at the boundaries of polytype inclusions.[11–13] MPs were supposed to nucleate at low-angle boundaries between a polytype inclusion and a matrix.[3,4,14] The evolution of polytype boundaries via the formation of microcracks was addressed by Siche *et al.*[15] They assumed that dislocation bundles in the basal plane, located within and near the MPs, and the stress concentrated at the MP surfaces might generate microcracks. This statement was supported by the results of optical and electron beam induced current investigations.[15] Recently, white beam topography,[6] Raman spectroscopy combined with optical microscopy,[16] transmission electron microscopy,[17] and scanning electron and optical microscopies with the aid of etching by molten KOH (Refs. 18 and 19) provided evidences for MP agglomeration at the boundaries of foreign polytype inclusions. Phase sensitive radiography, which has proven to be effective for the detection and mapping of MPs throughout the

crystal bulk, has demonstrated that closely spaced MPs interact and merge into pores.[20,21]

However, the mechanism by which MPs interact with the boundaries of foreign polytype inclusions, agglomerate, and coalesce into pores was not discussed in previous papers. Gutkin and co-workers[20,21] proposed that MPs diminish the orientational component of lattice mismatch between a polytype inclusion and a matrix and suggested a three-dimensional (3D) model of elastic interaction between MPs and inclusion boundaries.[22] What the model[22] lacks is that it does not take into account the inner cylindrical free surfaces of MPs whose effect must be significant for short-range interaction of MPs with the inclusion boundaries, as is the case with elastic interaction of MPs with each other.[13,23,24]

In the present paper, we provide experimental evidences to agglomeration of MPs into pores at the boundaries of foreign polytype inclusions and develop a two-dimensional (2D) model of elastic interaction between MPs and inclusion boundaries, which accounts for free surfaces of MPs.

II. EXPERIMENT

A. Crystals and techniques

SiC boule was grown in Ar by the sublimation sandwich method[4] on the carbon-terminated surface of 6*H*-SiC substrate in the presence of Sn vapor. The growth temperature was 2180 °C and the growth rate was 0.5 mm h^{-1}. The Sn vapor caused the transformation of the polytype of the substrate into 4*H*-SiC,[4] which was identified by x-ray diffractometry and white beam topography. To enhance luminescence in visible light range, crystal was N doped; the N pressure in the growth chamber was 133 mbar. The 0.4 mm thick wafers were cut off perpendicularly to the growth axis and mechanically polished on both sides.

The foreign polytype inclusions were revealed and identified by means of color photoluminescence (PL). Optical microscopy was performed on a Zeiss Universal microscope. Scanning electron microscopy (SEM) of the samples was done on JEOL JSM-6330F field emission SEM operating at 12 kV. MPs and macropores were studied using phase sensitive radiography at the 7B2 x-ray microscopy beamline of the Pohang Light Source, Korea. The energy of coherent beam from the source with the size 60 (H) × 160 (V) μm^2 continuously varied from 6 to 40 keV. A charge coupled device detector placed 34 m from the source had the matrix size of 1600 × 1200 pixels. The conversion of x rays into visible light was performed via $CdWO_4$ scintillator. The view field was switched between 4 and 0.5 mm horizontally, and the sample-to-detector distance was 6 cm.

B. Experimental results

Figure 1(a) shows a SEM image of typical pores located at the boundaries of foreign polytype inclusions. The PL image of Fig. 1(b) demonstrates the 6*H*-SiC inclusions in 4*H* matrix, as seen by the N activated luminescence taken at room temperature (yellow).[25] On a molten KOH treated surface, we observe slit pores that enclose smooth edges of the inclusions, as schematically illustrated in the inset of Fig. 1(a). Tubular pores are also seen at inclusion corners. Hexagonal etch pits near the inclusions represent MPs. The clearance of the slit pore is comparable with the MP diameters.

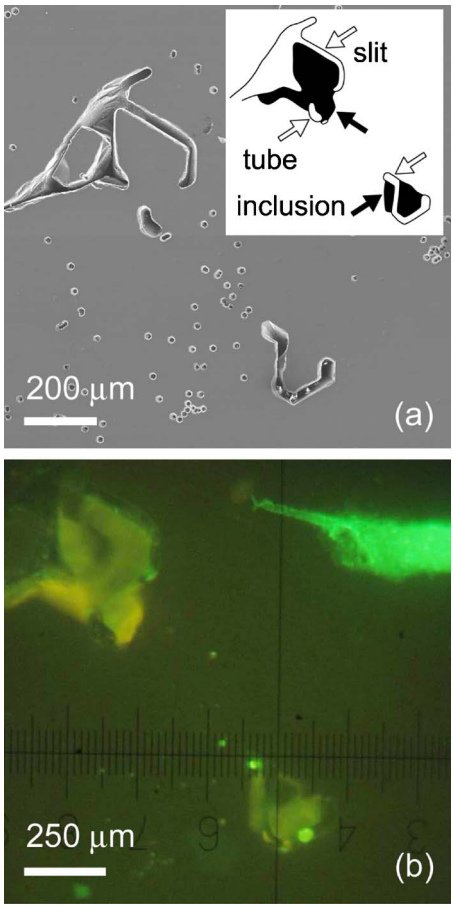

FIG. 1. (Color online) (a) SEM image of the pores bordering 6*H*-SiC inclusions in 4*H*-SiC wafer. The inset outlines the inclusions and the pores as pointed by black and white arrows, respectively. Hexagonal etch pits represent MPs. (b) PL image of the inclusions.

Similar features are also visible in the images of Fig. 2. Here, optical (a) and PL (b) micrographs of a big 6*H*-SiC inclusion in another 4*H*-SiC wafer are demonstrated. The inclusion exhibits a dendritic shape. The numbers listed from 1 to 4 indicate the corners of the dendrite. At the corners, tubular pores are partially and fully seen on the optical (a) and phase-radiographic (c) images, respectively. Note that the radiographic images of pore etch pits in Fig. 2(c) demonstrate the external regions of the pores on the wafer surface. In the phase radiography regime, by tilting the wafer around the axis perpendicular to the incident beam and parallel to the wafer surface, different projections of tubular pores were recorded. Using these projections, we confirm that the tubular pores penetrate the sample. Some of the tubes are joined together in the sample interior [see corners 3 and 4 in Fig. 2(c)].

MPs near the inclusion interact with the inclusion boundary, which is illustrated in the inset to Fig. 2(c). Here, the phase radiograph of a tube with a hexagonal cross section at an inclusion corner (labeled by 1) is shown. MPs bend to-

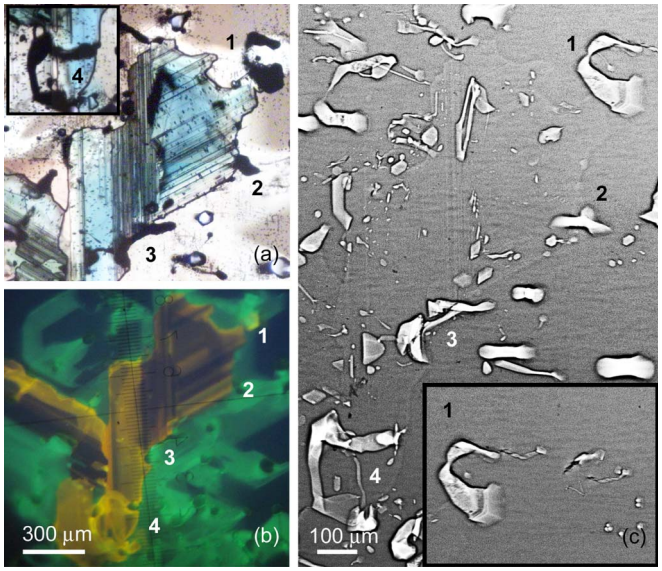

FIG. 2. (Color online) Dendritic 6*H*-SiC inclusion in 4*H*-SiC wafer: (a) optical micrograph; (b) PL image; and (c) phase radiograph. Numbers 1–4 indicate the inclusion corners where tubular pores are located. The inset to (a) shows the optical micrograph of the region indicated by 4 in (b) and (c). The inset to (c) displays the tube (indicated by 1) and the nearby MPs. The growth direction is nearly perpendicular to the sample surface.

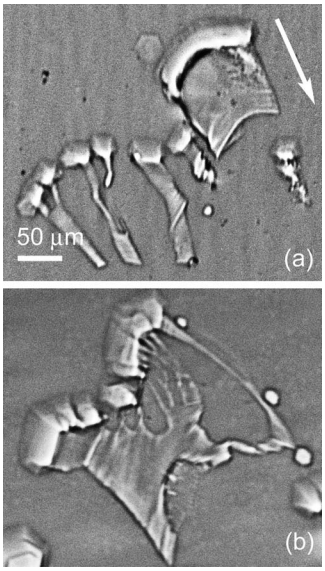

FIG. 3. Phase radiographs of slit pores located at the boundaries of 6*H*-SiC inclusions in 4*H*-SiC wafer; (a) bundling and merging of MPs near the pore; (b) the coalescence of MPs into the pore. White arrow in (a) represents the projection of the growth direction.

ward the tube and, at the same time, remarkably deviate from the growth direction, which is almost perpendicular to the sample surface. By evaluating the variation of the MP density, we confirmed that MPs were sparse around inclusions, while a high density of MPs was detected in inclusion-free regions throughout the wafer.

The observations of these foreign polytype inclusions and many other similar inclusions provide strong evidences for the attraction of MPs to the inclusion boundaries. These MPs may coalesce and form pores. Although generation of pores due to agglomeration of MPs originated from screw dislocations at the inclusion boundary cannot be ruled out, we believe that pore growth proceeds at the expense of MPs pulled out of the neighboring bulk. Tubular pores at inclusion corners are the first to form. (It should be noted that the term "tube" is used here to define a pore around an inclusion corner while the term "MP" is used to define a cylindrical pore formed in an arbitrary crystal area. As for MPs, the diameters of the tubular pores lie in the micrometer range, and so these pores are assumed either to form due to the coalescence of several MPs or to represent a single MP. The Burgers vector of these pores is added up from the Burgers vectors of the dislocations within the MPs merging to form a tubular pore and, if the inclusion boundary contains dislocations, the total Burgers vector of the dislocations lying in the fragment of the inclusion boundary removed by the tubular pore. Since different MPs have different Burgers vectors, the dislocation content of tubular pores can vary. Such pores can either contain dislocations or be dislocation-free.) Slit pores spread between tubular pores via joining the MPs aligned parallel to the borders of the slit pores.

The propagation of MPs together with the growth front is accompanied by their lateral motion toward the inclusion boundaries. This results in deviations of MPs from the growth direction. When MPs are inclined toward the inclusion, they become stepped, as exemplified in Fig. 3. Here, a pair of phase radiographs taken from the regions close to different 6*H*-SiC inclusions in the same 4*H*-SiC crystal is displayed. Twisting, bundling, and merging of MPs are clearly seen. The reactions of MPs provide strong evidence that MPs experience the influence of the stress fields produced by inclusion boundaries.[26]

III. THEORY

In this section, we propose a 2D model of elastic interaction between a MP and a polytype inclusion in SiC, which takes into account both dislocation charge and free surfaces of MPs, in contrast with our previous 2D and 3D models[22] which neglect the effect of MP free surfaces. Within this model, the MP and inclusion are supposed to lie in an isotropic infinite medium and are infinite along the z axis of the Cartesian coordinate system (x,y,z) (Fig. 4). The MP has a radius R_0, the coordinates of the MP axis are denoted by

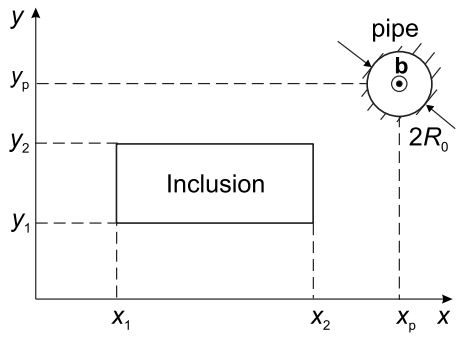

FIG. 4. Straight dislocated micropipe near a 2D inclusion.

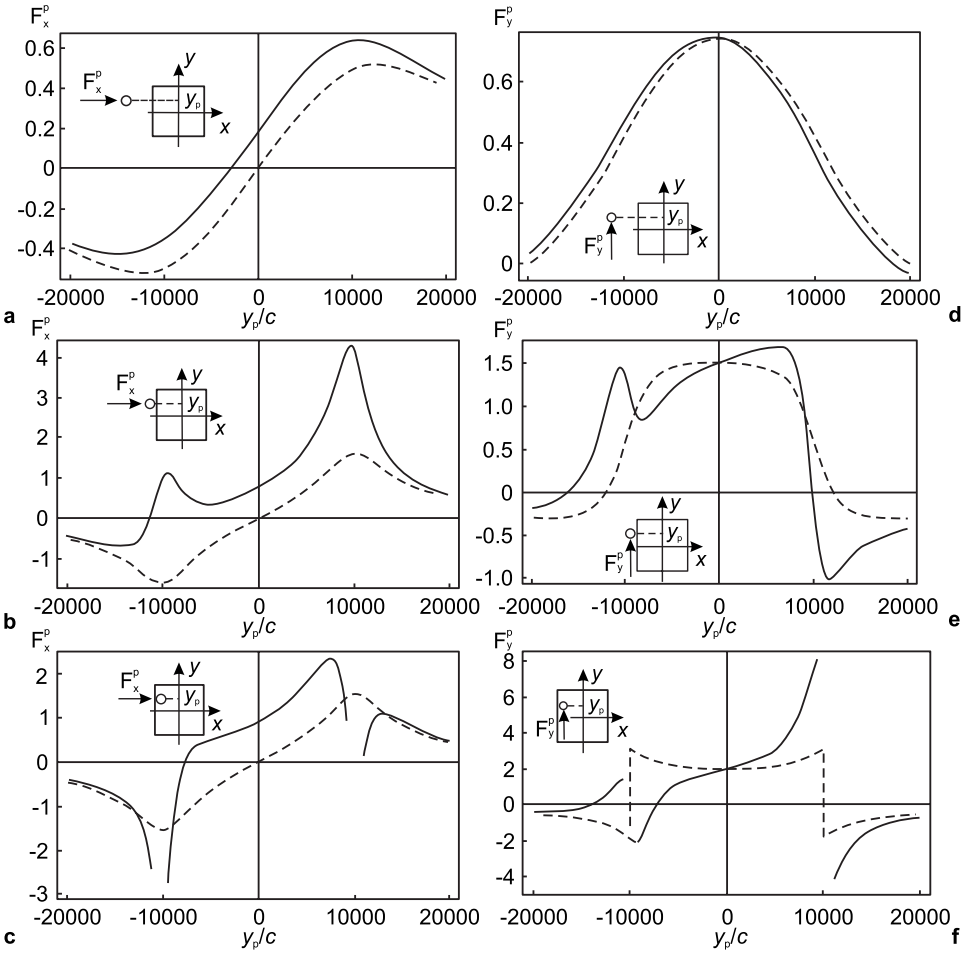

FIG. 5. The forces [(a)–(c)] F_x^p and [(d)–(f)] F_y^p exerted by an inclusion on a dislocated micropipe (continuous lines) and a screw dislocation without a micropipe (dashed lines) as functions of the dimensionless micropipe axis coordinate y_p/c for $b_z/c=8$, $x_1/c=y_1/c=-10\,000$, $x_2/c=y_2/c=10\,000$, $\nu=0.3$, $\beta_{xz}^{i*}=0.05$, and $\beta_{yz}^{i*}=0$; $R_0=1000c$ (continuous lines) and $R_0=0$ (dashed lines); [(a) and (d)] $x_p/c=-20\,000$, [(b) and (e)] $x_p/c=-12\,000$, and [(c) and (f)] $x_p/c=-8000$. c is the magnitude of an elementary Burgers vector. The forces are given in units of $\mu c/(4\pi)$. In (c) and (f), the forces acting on a dislocated micropipe (depicted by continuous lines) are not shown in the regions $|y_p-y_1|<R_0$ and $|y_p-y_2|<R_0$, where the micropipe intersects the inclusion boundary, because these forces are not calculated in these regions.

(x_p,y_p) and the Burgers vector of the MP dislocation is designated by $\mathbf{b}=b_z\mathbf{e}_z$. The inclusion occupies the region $(x_1<x<x_2, y_1<y<y_2, -\infty<z<\infty)$ and possesses two nonvanishing components, β_{xz}^{i*} and β_{yz}^{i*}, of plastic distortion. The plastic distortion components β_{xz}^{i*} and β_{yz}^{i*} may be introduced by free shears of the inclusion domain along the yz and xz planes, respectively, as is shown in detail in Ref. 22. These plastic distortions cause the corresponding elastic stresses both inside and around the inclusion, which can interact with the stress field of MPs.

For example, the component β_{xz}^{i*} may be introduced by a free shear of the inclusion domain along the yz plane. To provide such a shear, the inclusion domain is imaginarily extracted from the solid (matrix), freely sheared along the yz planes in the z direction by the angle β_{xz}^{i*} and embedded back into the matrix. As a result, the matrix also becomes distorted. If there is no plastic relaxation within the matrix and inclusion, both of them suffer elastic strains and stresses which are totally determined by the plastic distortion (antiplane eigenstrain) β_{xz}^{i*} and the inclusion geometry.[27]

We consider only pure plastic antiplane shear as the eigenstrain due to that, within our 2D model, any other eigenstrain component would create the elastic stress components which do not interact elastically with the superscrew dislocations contained in MPs. In that case, there would be only a short-range elastic attraction of MPs to the inclusion due to the image force of interaction between the inclusion and free cylindrical surfaces of MPs. We will investigate this image interaction as a special case of dislocation free MPs within our model. We believe these special results will remain qualitatively correct for any kind of the eigenstrain tensor.

Due to the interaction of the inclusion elastic stresses with the free surface of the MP and dislocation within it, the inclusion exerts a force $\mathbf{F}^p=F_x^p\mathbf{e}_x+F_y^p\mathbf{e}_y$ on the MP. The forces F_x^p and F_y^p equal to the projections of the force $\mathbf{F}^p$ on the x and y axes, respectively, are calculated in the Appendix. These forces are plotted in Figs. 5 and 6 for positive and negative signs of the MP dislocation, respectively as functions of the dimensionless MP axis coordinate y_p/c (where c is the magnitude of an elementary Burgers vector) at different values of the other MP axis coordinate x_p. The force F_x^p in (a) [(b) and (c), respectively] of Figs. 5 and 6 and the force F_y^p in (d) [(e) and (f), respectively] of Figs. 5 and 6 are plotted using the same parameter values. In Figs. 5(c), 5(f), 6(c), and 6(f), the continuous lines are not shown in the regions $|y_p-y_1|<R_0$ and $|y_p-y_2|<R_0$, where the MP intersects the inclusion boundary, because the corresponding forces are not calculated in these regions. It is seen from Figs. 5 and 6 that the forces F_x^p and F_y^p acting on a dislocation within a MP may significantly differ from the corresponding forces acting on a similar dislocation without a MP if the dislocation lies close to the inclusion boundary [see Figs. 5(b), 5(c), 5(e), 5(f), 6(b), 6(c), 6(e), and 6(f)]. The difference of the forces acting on the dislocation within a MP and

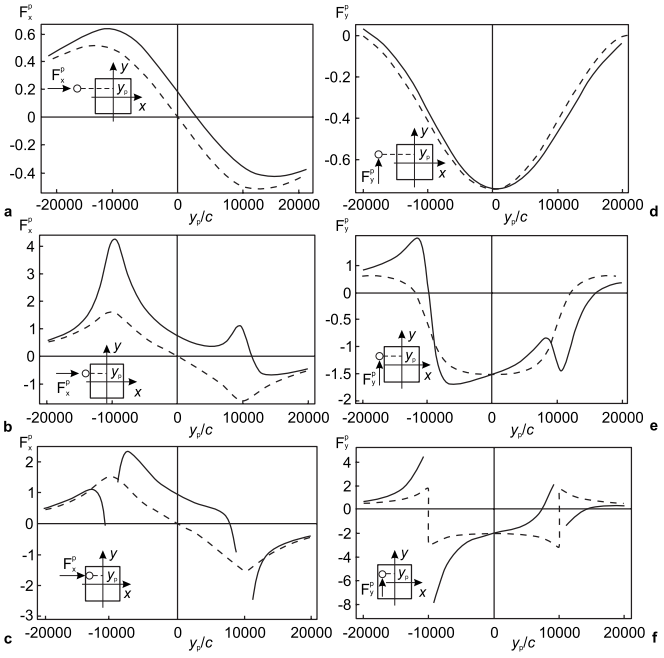

FIG. 6. The forces [(a)–(c)] F_x^p and [(d)–(f)] F_y^p exerted by an inclusion on a dislocated micropipe (continuous lines) and a screw dislocation without a micropipe (dashed lines) as functions of the dimensionless micropipe axis coordinate y_p/c for $b_z/c=-8$, $x_1/c=y_1/c=-10\,000$, $x_2/c=y_2/c=10\,000$, $\nu=0.3$, $\beta_{xz}^{i*}=0.05$, and $\beta_{yz}^{i*}=0$; $R_0=1000c$ (continuous lines) and $R_0=0$ (dashed lines); [(a) and (d)] $x_p/c=-20\,000$, [(b) and (e)] $x_p/c=-12\,000$, and [(c) and (f)] $x_p/c=-8000$. c is the magnitude of an elementary Burgers vector. The forces are given in units of $\mu c/(4\pi)$. In (c) and (f), the forces acting on a dislocated micropipe (depicted by continuous lines) are not shown in the regions $|y_p-y_1|<R_0$ and $|y_p-y_2|<R_0$, where the micropipe intersects the inclusion boundary, because these forces are not calculated in these regions.

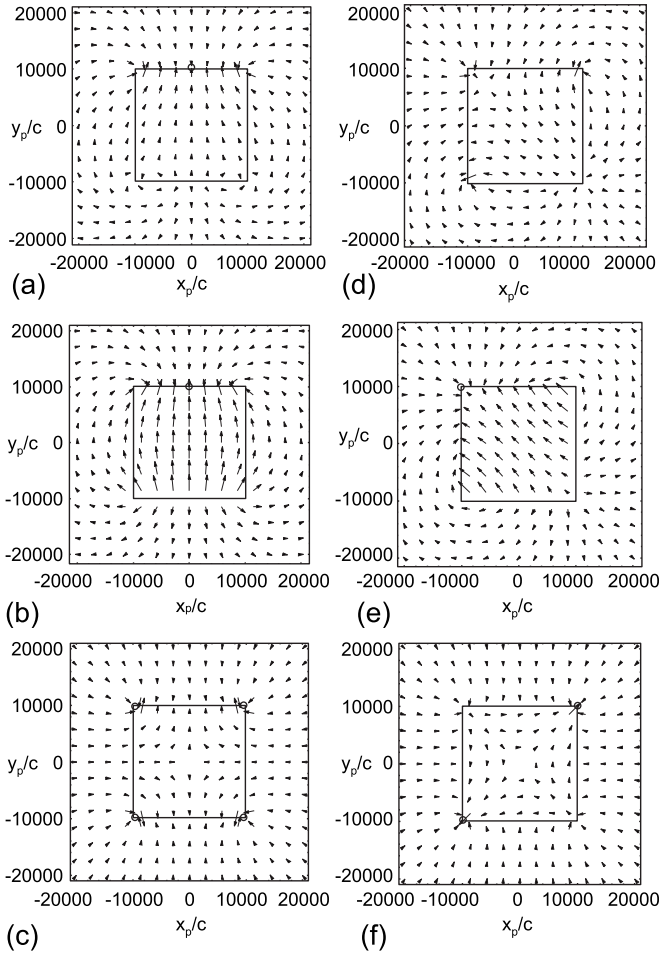

FIG. 7. The forces $\mathbf{F}^p$ acting on a [(a) and (d)] dislocated micropipe, [(b) and (e)] screw dislocation without a micropipe, and [(c) and (f)] micropipe without a dislocation. The arrows indicate the force directions, and their length is proportional to the force magnitude. The large rectangles show the cross sections of the inclusion boundaries. The circles show equilibrium positions of the (a) dislocated micropipe, [(b) and (e)] screw dislocation, or [(c) and (f)] dislocation-free micropipe. The figures are displayed for the following parameter values: $x_1/c=y_1/c=-10\,000$, $x_2/c=y_2/c=10\,000$, and $\nu=0.3$; [(a)–(c)] $\beta_{xz}^{i*}=0.05$ and $\beta_{yz}^{i*}=0$ and [(d)–(f)] $\beta_{xz}^{i*}=\beta_{yz}^{i*}=0.05$; [(a), (b), (d), and (e)] $b_z/c=8$ and [(c) and (f)] $b_z=0$; [(a), (c), (d), and (f)] $R_0=1000c$ and [(b) and (e)] $R_0=0$.

that without a MP is particularly strong in the vicinities of inclusion corners. However, the variance of these forces diminishes as the dislocation moves away from the inclusion boundary [see Figs. 5(a), 5(d), 6(a), and 6(d)].

In the following, besides dislocated MPs and dislocations without MPs, we consider dislocation-free MPs. Such MPs may exist as nonequilibrium structures due to the coalescence of two MPs with opposite Burgers vectors. The vector fields of the force $\mathbf{F}^p=(F_x^p,F_y^p)$ acting on the dislocated MP (dislocation without a MP and dislocation-free MP) are shown in Figs. 7(a) and 7(d) [Figs. 7(b) and 7(e), and Figs. 7(c) and 7(f)], respectively, in the coordinate space $(x_p/c,y_p/c)$ for the cases $\beta_{xz}^{i*}=0.05$ and $\beta_{yz}^{i*}=0$ [Figs. 7(a)–7(c)] and $\beta_{xz}^{i*}=\beta_{yz}^{i*}=0.05$ [Figs. 7(d)–7(f)]. Comparison of Figs. 7(a) and 7(b) shows that although the magnitudes and directions of the forces $\mathbf{F}^p$, calculated for the cases of a dislocated MP and dislocation without a MP, differ near the inclusion boundaries, the overall pictures of the vector fields in the two cases are similar, and the dislocation equilibrium positions in both the cases are the same and are located at the center of one of the facets. Similar pictures of vector fields are also seen in Figs. 7(d) and 7(e). [It should, however, be noted that in Fig. 7(e), the equilibrium dislocation position is at the inclusion corner, while in Fig. 7(d), it lies at another point of the inclusion boundary. The exact position of this point cannot, however, be determined from Fig. 7(d) and requires a separate calculation of the force acting on the dislocated MP at the inclusion boundaries. This calculation is beyond the scope of our paper.] In contrast, the equilibrium positions of a dislocation-free MP lie at the inclusion corners [see Figs. 7(c) and 7(f)]. Thus, from Fig. 7, it follows that the equilibrium positions of a dislocated MP lie at the inclusion boundary, but the exact equilibrium position of a dislocated MP at the inclusion boundary is determined by a balance of the force acting on the cavity (which attracts it to the inclusion corner) and the force acting on a MP dislocation (which attracts it to other points of the inclusion boundary).

IV. SUMMARY

Using synchrotron phase sensitive radiography, optical and scanning electron microscopies, and color photoluminescence, we have revealed and identified foreign polytype inclusions in SiC. We have shown that MPs are attracted to their boundaries due to the action of inclusion and MP stress fields. The accumulation of MPs at the boundaries of polytype inclusions has been shown to result in their merging into pores. We have explained the observations within a 2D model of MP-inclusion interaction and calculated the forces exerted on MPs by a foreign polytype inclusion with a rigorous account for both inclusion and MP dislocation stress fields, as well as MP surfaces. The calculations demonstrated that the equilibrium positions of MPs lie at polytype inclusion boundaries.

ACKNOWLEDGMENTS

This research is supported by the Creative Research Initiatives (Functional X-ray Imaging) of MOST/KOSEF, BK21 Korea, Russian Fund of Basic Research (Grants No. 04-01-00211 and No. 06-02-16244), Russian Science Support Foundation, Federal Agency of Science and Innovations (grant of the President of the Russian Federation, MK-8340.2006.1), National Science Council (Taiwan), and Swiss Fonds National de la Recherche Scientifique.

APPENDIX: INTERACTION FORCE BETWEEN TWO-DIMENSIONAL INCLUSION AND DISLOCATED MICROPIPE

In this appendix, we calculate the force exerted by the 2D inclusion shown in Fig. 4 on the dislocated MP displayed in the same figure. As will be shown below, the interaction force between the dislocated MP and inclusion may be presented as the sum of two terms. The first one is the dislocation-inclusion interaction force, which would act in the absence of the MP. This force was calculated before for both the 2D and 3D cases.[22] The second term takes into account the presence of the cavity and may be interpreted as an image force applied within the cavity.

To calculate the total force exerted by the inclusion on the MP, we consider the effect of the cavity surface on the inclusion stress field. For this purpose, we present the total inclusion stress field σ_{ij}^{i} in the form $\sigma_{ij}^{i}=\sigma_{ij}^{i\infty}+\sigma_{ij}^{\nu}$, where $\sigma_{ij}^{i\infty}$ is the stress field of the inclusion in the absence of the MP and σ_{ij}^{ν} is an extra inclusion stress field associated with the presence of the MP. This stress field is necessary to satisfy the free-traction condition at the MP surface. Hereafter, in the calculation of the MP-inclusion interaction force, we will not need the explicit expression for the stress $\sigma_{ij}^{i\infty}$, and so we restrict ourselves by computing the stress σ_{ij}^{ν}.

In the following, we consider the case where the MP does not intersect the inclusion boundary. In this case, to cast σ_{ij}^{ν}, we model the inclusion by virtual screw dislocations continuously distributed over the inclusion interface (Fig. 8). The first two continuous ensembles of virtual screw dislocations are distributed within the interval $x_1<x<x_2$ over the inclusion facets $y=y_1$ and $y=y_2$. The dislocations of these two ensembles have infinitesimal Burgers vectors $\mathbf{b}_s=b_s\mathbf{e}_z$ and $-\mathbf{b}_s=-b_s\mathbf{e}_z$, respectively, and are distributed with the linear density $\rho_1=\beta_{xz}^{i*}/b_s$. The other two dislocation ensembles are distributed over the inclusion facets $x=x_2$ and $x=x_1$ within the interval $y_1<y<y_2$. The dislocations of these two ensembles also have infinitesimal Burgers vectors $\mathbf{b}_s$ and $-\mathbf{b}_s$, respectively, but their distribution density $\rho_2=\beta_{yz}^{i*}/b_s$ differs from that of the first two dislocation ensembles. Using the definition[27] of dislocation plastic distortion, one can see that the total plastic strain induced by the four virtual dislocation ensembles that model the inclusion is equal to the plastic strain of this inclusion.

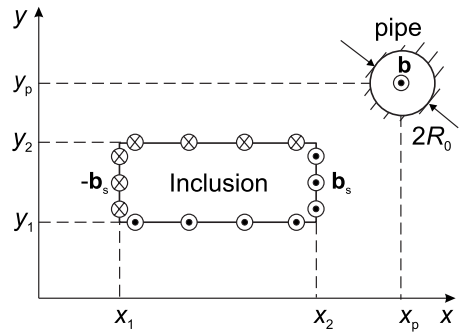

FIG. 8. Inclusion and its representation as four continuous arrays of virtual screw dislocations distributed over the inclusion facets.

The total inclusion stress field may then be presented as

$$\sigma_{ij}^{i} = -\ \rho_1\int_{x_1}^{x_2}\sigma_{ij}^{d}(x,x',y,y')dx'\Big|_{y'=y_1}^{y'=y_2} + \rho_2\int_{y_1}^{y_2}\sigma_{ij}^{d}(x,x',y,y')dy'\Big|_{x'=x_1}^{x'=x_2}, \tag{A1}$$

where $\sigma_{ij}^{d}(x,x',y,y')$ is the stress field of a virtual screw dislocation with the Burgers vector $\mathbf{b}_s$ lying at the line $(x=x',\ y=y')$.

The stress field σ_{ij}^{d} of the above virtual screw dislocation in the presence of the MP may be written as the sum of the stress field $\sigma_{ij}^{d\infty}(x-x',y-y',b_s)$ that such a dislocation would create in an infinite medium and the two stress fields, $\sigma_{ij}^{d\infty}(x-x_p,y-y_p,b_s)$ and $-\sigma_{ij}(x-x_{im},y-y_{im},b_s)$, of two image screw dislocations, the first lying at the MP axis and having the Burgers vector $\mathbf{b}_s$ and the second lying within the cavity at the line $(x=x_{im},\ y=y_{im})$ and having the Burgers vector $-\mathbf{b}_s$. The line $(x=x_{im},\ y=y_{im})$ of the second image dislocation is located at the plane that joins the virtual dislocation and the MP axis at the distance $d-R_0^2/d$ from the virtual dislocation, where d is the distance between the virtual dislocation and the MP axis[28] (Fig. 9). The image dislocations make the MP surface traction-free, providing the condition $\sigma_{nz}=0$ (where $\mathbf{n}$ is the normal to the MP surface) at any point of this surface. Thus, using the expressions[29] for the nonvanishing stress components $\sigma_{xz}^{d\infty}$ and $\sigma_{yz}^{d\infty}$ of a screw dislocation, which is placed at the origin of a Cartesian coordinate system in an isotropic infinite medium,

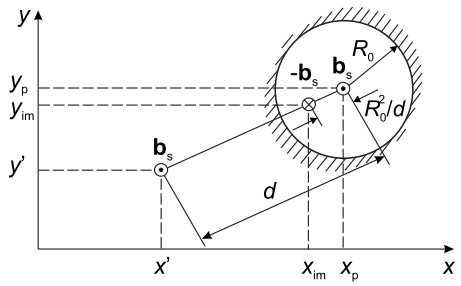

FIG. 9. Screw dislocation near a cylindrical cavity. Two image dislocations within the cavity provide the meeting of the free-traction conditions at the cavity surface.

$$\sigma_{xz}^{d\infty}(x,y,b_s) = -\frac{\mu b_s y}{2\pi(x^2+y^2)}, \quad \sigma_{yz}^{d\infty}(x,y,b_s) = \frac{\mu b_s x}{2\pi(x^2+y^2)}, \tag{A2}$$

and employing the relations

$$x_{im} = x_p - \frac{(x_p - x')R_0^2}{(x_p - x')^2 + (y_p - y')^2}, \quad y_{im} = y_p - \frac{(y_p - y')R_0^2}{(x_p - x')^2 + (y_p - y')^2}, \tag{A3}$$

we obtain

$$\sigma_{xz}^{d} = \sigma_{xz}^{d\infty}(x-x', y-y') + \sigma_{xz}^{d\infty}(x-x_p, y-y_p) + \frac{\mu b_s}{2\pi}\frac{\hat{y}(\bar{x}^2+\bar{y}^2) - \bar{y}R_0^2}{P^4}, \tag{A4}$$

$$\sigma_{yz}^{d} = \sigma_{yz}^{d\infty}(x-x', y-y') + \sigma_{yz}^{d\infty}(x-x_p, y-y_p) - \frac{\mu b_s}{2\pi}\frac{\hat{x}(\bar{x}^2+\bar{y}^2) - \bar{x}R_0^2}{P^4}, \tag{A5}$$

where $\hat{x}=x-x_p$, $\hat{y}=y-y_p$, $\bar{x}=x'-x_p$, $\bar{y}=y'-y_p$, and $P^4=(\bar{x}^2+\bar{y}^2)(\hat{x}^2+\hat{y}^2)-2R_0^2(\bar{x}\hat{x}+\bar{y}\hat{y})+R_0^4$. The first terms in formulas (A4) and (A5) denote the infinite-medium stress field of the virtual dislocation shifted from the origin of the coordinate system, the second terms identify the stress components of the image dislocation lying at the MP axis, while the third terms, written explicitly, stand for the stress components of the image dislocation situated at the line $(x=x_{im}, y=y_{im})$.

To obtain the stress field of the inclusion, we substitute expressions (A4) and (A5) to formula (A1) for the inclusion stress field σ_{ij}^{i}. Then, after integration, the total infinite-medium stress fields of all the virtual dislocations will yield the infinite-medium $\sigma_{ij}^{i\infty}$ field of the inclusion, the terms associated with the image dislocations at the MP axis will provide zero, and the terms describing the stresses of the image dislocations at the points $(x=x_{im}, y=y_{im})$ will give the inclusion image stress field σ_{ij}^{ν}. Thus, insertion of Eqs. (A4) and (A5) to Eq. (A1) gives $\sigma_{ij}^{i}=\sigma_{ij}^{i\infty}+\sigma_{ij}^{\nu}$, where $\sigma_{ij}^{\nu}=\tilde{\sigma}_{ij}^{\nu}\big|_{\tilde{x}=\tilde{x}_1}^{\tilde{x}_2}\big|_{\tilde{y}=\tilde{y}_1}^{\tilde{y}_2}$. Here, $\tilde{x}_1=x_1-x_p$, $\tilde{x}_2=x_2-x_p$, $\tilde{y}_1=y_1-y_p$, and $\tilde{y}_2=y_2-y_p$, as above, and the only two nonvanishing components of the tensor $\tilde{\sigma}_{ij}^{\nu}$ are given by

$$\tilde{\sigma}_{xz}^{\nu}(x_1,x_2) = \frac{\mu R_0^2}{2\pi(\hat{x}^2+\hat{y}^2)^2}\left\{-\beta_{xz}^{i*}\left[\hat{x}\hat{y}\ln P^4 + (\hat{y}^2 - \hat{x}^2)\arctan\frac{Q_1}{Q_2}\right] + \beta_{yz}^{i*}\left(\frac{\hat{y}^2-\hat{x}^2}{2}\ln P^4 + 2\hat{x}\hat{y}\arctan\frac{Q_2}{Q_1}\right)\right\}, \tag{A6}$$

$$\tilde{\sigma}_{yz}^{\nu}(x,y) = -\frac{\mu R_0^2}{2\pi(\hat{x}^2+\hat{y}^2)^2}\left\{-\beta_{xz}^{i*}\left(\frac{\hat{x}^2-\hat{y}^2}{2}\ln P^4 + 2\hat{x}\hat{y}\arctan\frac{Q_1}{Q_2}\right) + \beta_{yz}^{i*}\left[\hat{x}\hat{y}\ln P^4 + (\hat{x}^2 - \hat{y}^2)\arctan\frac{Q_2}{Q_1}\right]\right\}, \tag{A7}$$

where $Q_1=\bar{x}(\hat{x}^2+\hat{y}^2)-\hat{x}R_0^2$ and $Q_2=\bar{y}(\hat{x}^2+\hat{y}^2)-\hat{y}R_0^2$.

Now, we can find the force F_k^p $(k=x,y)$ exerted by the inclusion on the dislocated MP. For this purpose, first, we write down the expression for the total strain energy W of a crystal with the inclusion and the dislocated MP. The energy W may be presented as

$$W = W_d + W_{d\text{-}i} + W_i, \tag{A8}$$

where W_d is the self-energy of the screw dislocation within the MP (which does not depend on the MP axis coordinates x_p and y_p), $W_{d\text{-}i}$ is the energy of the interaction between the inclusion and the dislocation stress field σ_{ij}^{p}, and W_i is the self-energy of the inclusion in the presence of the cylindrical cavity. [The stress field σ_{ij}^{p} of a screw dislocation with the Burgers vector $b_p\mathbf{e}_z$, located within a cylindrical cavity with the axis $(x=x_p, y=y_p)$, coincides with the stress field, which such a dislocation lying at the line $(x=x_p, y=y_p)$ would create in an infinite medium: $\sigma_{ij}^{p}(x,y)=\sigma_{ij}^{d\infty}(\hat{x},\hat{y},b_p)$.] The energy W_i (per unit inclusion length in the z direction) may be written as[30]

$$W_i = -\frac{1}{2}\int_{S_i}\sigma_{ij}^{i}\beta_{ji}^{i*}dS, \tag{A9}$$

where S_i is the region $(x_1<x<x_2, y_1<y<y_2)$ of the inclusion cross section and S is the integration parameter. Using the relation $\sigma_{ij}^{i}=\sigma_{ij}^{i\infty}+\sigma_{ij}^{\nu}$, we rewrite formula (A9) in the form $W_i=W_i^{\infty}+W_i'$, where

$$W_i^{\infty} = -\frac{1}{2}\int_{S_i}\sigma_{ij}^{i\infty}\beta_{ji}^{i*}dS \tag{A10}$$

is the proper energy of the inclusion in an infinite medium (which does not depend on the coordinates x_p and y_p) and

$$W_i' = -\frac{1}{2}\int_{S_i}^{-}\sigma_{ij}^{\nu}\beta_{ji}^{i*}dS \tag{A11}$$

is the contribution of the cavity to the inclusion self-energy. Comparison of formula (A11) with the general formula[30]

$$W_{i\text{-}\sigma}(\sigma_{ij}^{e}) = -\int_{S_i} \sigma_{ij}^{e}\beta_{ji}^{i*}dS \tag{A12}$$

for the energy $W_{i\text{-}\sigma}$ (per unit inclusion length in the z direction) of the inclusion interaction with an arbitrary external stress field σ_{ij}^{e} shows that $W_i' = W_{i\text{-}\sigma}(\sigma_{ij}^{v}/2)$. Thus, W_i' is equal to the energy of the interaction between the inclusion and the virtual external stress field $\sigma_{ij}^{v}/2$. Besides, since the quantity $W_{d\text{-}i}$ describes the energy of the interaction between the inclusion and the dislocation stress field σ_{ij}^{p}, the quantity $W_{d\text{-}i} + W_i'$ is equal to the energy of the inclusion interaction with the effective applied stress $\tilde{\sigma}_{ij}^{e} = \sigma_{ij}^{p} + \sigma_{ij}^{v}/2$.

The above considerations allow one to calculate the force F_k^p $(k=x,y)$ exerted by the inclusion on the dislocated MP without a preliminary derivation of explicit expressions for the system energy. Indeed, from formula (A8) and the relation $W_i = W_i^{\infty} + W_i'$, it follows that the energy W may be presented as $W = W_d + W_i^{\infty} + W_{d\text{-}i} + W_i'$. The first two terms in the latter expression do not depend on the MP axis coordinates x_p and y_p. As a result, we have $F_x^p = -\partial W/\partial x_p = -\partial(W_{d\text{-}i} + W_i')/\partial x_p$, $F_y^p = -\partial W/\partial y_p = -\partial(W_{d\text{-}i} + W_i')/\partial y_p$. Because the sum $W_{d\text{-}i} + W_i'$ may be interpreted as the energy of the inclusion interaction with the effective external stress $\tilde{\sigma}_{ij}^{e}$, the force F_k^p is equal to the force which inclusion would exert on a source of the stress field $\tilde{\sigma}_{ij}^{e}$. In turn, the force $-F_k^p$ exerted by the dislocated MP on the inclusion is equal to the force exerted on the inclusion by the effective stress field $\tilde{\sigma}_{ij}^{e}$. Modeling the inclusion by virtual screw dislocations continuously distributed over the inclusion interface with linear densities ρ_1 and ρ_2 (Fig. 8), we present the force $-F_k^p$ as

$$-F_k^p = -\rho_1 \int_{x_1}^{x_2} F_k^d(x,y)dx \Big|_{y=y_1}^{y_2} + \rho_2 \int_{y_1}^{y_2} F_k^d(x,y)dy \Big|_{x=x_1}^{x_2}, \tag{A13}$$

where F_k^d is the force with which the effective stress field $\tilde{\sigma}_{ij}^{e}$ acts on a virtual dislocation with the Burgers vector $b_s\mathbf{e}_z$, lying at the line (x,y). Insertion of the Peach-Koehler formulas[29]

$$F_x^d = b_s\tilde{\sigma}_{yz}^{e}, \quad F_y^d = -b_s\tilde{\sigma}_{xz}^{e} \tag{A14}$$

and the equalities $\rho_1 = \beta_{xz}^{i*}/b_s$ and $\rho_2 = \beta_{yz}^{i*}/b_s$ to formula (A13) yields the following expressions for the forces F_x^p and F_y^p:

$$F_x^p = -\left[-\beta_{xz}^{i*}\int \tilde{\sigma}_{yz}^{e}(x,y)d\hat{x} + \beta_{yz}^{i*}\int \tilde{\sigma}_{yz}^{e}(x,y)d\hat{y}\right]\Big|_{\hat{x}=\tilde{x}_1}^{\tilde{x}_2}\Big|_{\hat{y}=\tilde{y}_1}^{\tilde{y}_2}, \tag{A15}$$

$$F_y^p = \left[-\beta_{xz}^{i*}\int \tilde{\sigma}_{xz}^{e}(x,y)d\hat{x} + \beta_{yz}^{i*}\int \tilde{\sigma}_{xz}^{e}(x,y)d\hat{y}\right]\Big|_{\hat{x}=\tilde{x}_1}^{\tilde{x}_2}\Big|_{\hat{y}=\tilde{y}_1}^{\tilde{y}_2}. \tag{A16}$$

Substituting the relations $\tilde{\sigma}_{ij}^{e} = \sigma_{ij}^{p} + \sigma_{ij}^{v}/2$ and $\sigma_{ij}^{p}(x,y) = \sigma_{ij}^{d\infty}(\hat{x},\hat{y},b_z)$ and formulas (A2), (A6), and (A7) for $\sigma_{ij}^{d\infty}$ and σ_{ij}^{v} to formulas (A15) and (A16), and performing integration, after lengthy calculations, one obtains explicit analytical expressions for the forces F_x^p and F_y^p. Because these expressions are very cumbersome, we do not give them here.

*Author to whom correspondence should be addressed; jhje@postech.ac.kr

[1] Y. M. Tairov and V. F. Tsvetkov, J. Cryst. Growth **43**, 209 (1978).
[2] R. A. Stein and P. Lanig, J. Cryst. Growth **131**, 71 (1993).
[3] G. Augustine, H. McD. Hobgood, V. Balakrishna, G. Dunne, and R. H. Hopkins, Phys. Status Solidi B **202**, 137 (1997).
[4] Yu. A. Vodakov, A. D. Roenkov, M. G. Ramm, E. N. Mokhov, and Yu. N. Makarov, Phys. Status Solidi B **202**, 177 (1997).
[5] R. Yakimova, M. Syvajarvi, T. Iakimov, H. Jacobsson, R. Raback, A. Vehanen, and E. Janzen, J. Cryst. Growth **217**, 255 (2000).
[6] R. Madar, E. Pernot, M. Anikin, and M. Pons, J. Phys.: Condens. Matter **14**, 13009 (2002).
[7] G. V. Saparin, E. N. Mokhov, S. K. Obyden, and A. D. Roenkov, Scanning **18**, 25 (1996).
[8] K. Semmelroth, N. Schulze, and G. Pensl, J. Phys.: Condens. Matter **16**, S1597 (2004).
[9] M. Katsuno, N. Ohtani, T. Aigo, T. Fujimoto, H. Tsuge, H. Yashiro, and M. Kanaya, J. Cryst. Growth **216**, 256 (2000).
[10] X. R. Huang, M. Dudley, W. M. Vetter, W. Huang, S. Wang, and C. H. Carter, Appl. Phys. Lett. **74**, 353 (1999).
[11] N. Ohtani, T. Fujimoto, M. Katsuno, T. Aigo, and H. Yashiro, J. Cryst. Growth **237-239**, 1180 (2002).
[12] E. N. Mokhov, M. G. Ramm, A. D. Roenkov, and Yu. A. Vodakov, Mater. Sci. Eng., B **46**, 317 (1997).
[13] M. Yu. Gutkin, A. G. Sheinerman, T. S. Argunova, E. N. Mokhov, and J. H. Je, Proc. SPIE **5831**, 125 (2005).
[14] J. Heindl, H. P. Strunk, V. D. Heydemann, and G. Pensl, Phys. Status Solidi A **162**, 251 (1997).
[15] D. Siche, H.-J. Rost, J. Doerschel, D. Schulz, and J. Wollweber, J. Cryst. Growth **237-239**, 1187 (2002).
[16] S. Ferrero *et al.*, J. Phys.: Condens. Matter **14**, 13397 (2002).
[17] A. Mantzari, E. K. Polychroniadis, J. Wollweber, A. Freudenberg, C. Balloud, and J. Camassel, J. Cryst. Growth **275**, e1813 (2005).
[18] L. N. Zhu, H. Li, B. Q. Hu, X. Wu, and X. L. Chen, J. Phys.: Condens. Matter **17**, L85 (2005).
[19] S. Wang, E. Sanchez, A. Kopec, M. Zhang, and O. Hernandez, Mater. Sci. Forum **457-460**, 51 (2004).
[20] M. Yu. Gutkin, A. G. Sheinerman, T. S. Argunova, E. N. Mokhov, J. H. Je, Y. Hwu, and W. L. Tsai, Mater. Sci. Forum **457-460**, 367 (2004).
[21] T. S. Argunova, L. M. Sorokin, L. S. Kostina, J. H. Je, M. Yu. Gutkin, and A. G. Sheinerman, Crystallogr. Rep. **49**, S33 (2004).
[22] M. Yu. Gutkin *et al.*, J. Appl. Phys. **100**, 093518 (2006).
[23] M. Yu. Gutkin and A. G. Sheinerman, Phys. Status Solidi B **231**, 256 (2002).
[24] M. Yu. Gutkin, A. G. Sheinerman, T. S. Argunova, J. H. Je, H. S.

Kang, Y. Hwu, and W. L. Tsai, J. Appl. Phys. **92**, 889 (2002).
[25] G. V. Saparin, S. K. Obyden, P. V. Ivannikov, E. B. Shishkin, E. N. Mokhov, A. D. Roenkov, and D. H. Hofmann, Scanning **19**, 269 (1997).
[26] M. Yu. Gutkin, A. G. Sheinerman, T. S. Argunova, E. N. Mokhov, J. H. Je, Y. Hwu, W. L. Tsai, and G. Margaritondo, J. Appl. Phys. **94**, 7076 (2003).
[27] T. Mura, *Micromechanics of Defects in Solids* (Martinus Nijhoff, Dordrecht, 1987).
[28] J. Dundurs, in *Recent Advances in Engineering Science*, edited by A. C. Eringen (Gordon and Breach, New York, 1967), Vol. 2, p. 223.
[29] J. P. Hirth and J. Lothe, *Theory of Dislocations* (Wiley, New York, 1982).
[30] T. Mura, in *Advances in Materials Research*, edited by H. Herman (Interscience, New York, 1968), Vol. 3, p. 1.